Three-dimensional particle-in-cell simulation of a miniature plasma source for a microwave discharge ion thruster

Takao, Yoshinori; Koizumi, Hiroyuki; Komurasaki, Kimiya; Eriguchi, Koji; Ono, Kouichi

Three-dimensional particle-in-cell simulation of a miniature plasma source for a microwave discharge ion thruster

Yoshinori Takao[1a], Hiroyuki Koizumi[2], Kimiya Komurasaki[3], Koji Eriguchi[1] and Kouichi Ono[1]

[1] Department of Aeronautics and Astronautics, Kyoto University, Kyoto-daigaku Katsura, Nishikyo-ku, Kyoto 615-8540, Japan

[2] Research Centre for Advanced Science and Technology, The University of Tokyo, 4-6-1 Komaba, Meguro-ku, Tokyo 153-8904, Japan

[3] Department of Advanced Energy, The University of Tokyo, 5-1-5 Kashiwanoha, Kashiwa, Chiba 277-8583, Japan

E-mail: ystakao@gmail.com

Abstract

We have developed a three-dimensional particle model for a miniature microwave discharge ion thruster to elucidate the mechanism of ECR discharges confined in a small space. The model consists of a particle-in-cell simulation with a Monte Carlo collision algorithm (PIC-MCC) for the kinetics of charged particles, a finite-difference time-domain method for the electromagnetic fields of 4.2-GHz microwaves, and a finite element analysis for the

[a] Present address: Division of Systems Research, Faculty of Engineering, Yokohama National University, 79-5 Tokiwadai, Hodogaya-ku, Yokohama 240-8501, Japan.
E-mail: takao@ynu.ac.jp

magnetostatic fields of permanent magnets. The PIC-MCC results have shown that the electrons are well confined owing to the mirror magnetic fields and can be effectively heated in the ECR layer downstream of a ring-shaped antenna. The confinement results in the ring-shaped profiles of the plasma density along the antenna. The visual appearance of the plasma discharge of the thruster in operation was also ring-shaped. Moreover, the ions are expected to be accelerated effectively through the grid electrode without a large loss of ions toward side walls, that is, the plasma source developed here would be desirable in ion thrusters.

Keywords: micro ion thruster, ECR plasma, microwave, xenon, particle-in-cell/Monte Carlo

Submitted to: *Plasma Sources Sci. Technol.*

1. Introduction

In recent years, the worldwide interest in microspacecraft has grown to such an extent that even universities are currently able to launch and operate microspacecraft because of their low costs and short development periods. However, most microspacecraft do not have any propulsion systems, which is why they rely on passive controls, such as gravity gradient stabilization and magnetic torquers. If a microspacecraft had microthrusters mounted on it, we could control the microspacecraft more effectively to create a specific flight path. Owing to the limited power generation and propellant storage, high specific impulses, high-thrust efficiencies and low-power consumptions are required for microthrusters, in addition to small size and light weight [1].

Figure 1 shows a miniature ion thruster developed by the Institute of Space and Astronautical Science in Japan Aerospace Exploration Agency (ISAS/JAXA) with the purpose of solving the issues mentioned above [2, 3]; the ion thruster is referred to as μ1 (“mu-one”), as one of the “mu-series” microwave discharge ion thrusters developed by ISAS/JAXA, where electron cyclotron resonance (ECR) is employed for plasma discharges [4, 5]. Its ion source has the 250 W/A ion production cost and 37% mass utilization efficiency for 1.0 W microwave input power and 14.6 μg/s xenon mass flow, where the neutralizer employs the identical discharge chamber and operates with a gas flow of half ion beam source. By using an ion beam source and a neutralizer, a miniature ion propulsion system (MIPS) was developed by the University of Tokyo in collaboration with the Next Generation Space

System Technology Research Association (NESTRA) in Japan. The engineering model specifications of the MIPS is evaluated at the weight of 8.1 kg (dry: 7.1 kg), volume of 39 cm × 26 cm × 15 cm, power consumption of 39 W and thrust of 300 μN with specific impulse of 1200 s [6]. The MIPS is installed on a 50 kg-class spacecraft, HODOYOSHI-4, which was developed under the Japanese government funded project, “New Paradigm of Space Development and Utilization by Nano-satellite”, and was launched by RS-20 rocket (Dnepr Launch Vehicle) from Yasny Launch Base, Russia, on June 19, 2014. The MIPS will be the world’s first ion thruster system operated in space for 50 kg-class nano-satellites.

On the other hand, there are still some physical phenomena to be elucidated in the miniature ion thruster μ1; thus, the development of μ1 is currently dependent on some empirical designs. In order to clarify the mechanism of ECR discharges in a small space and to provide clear guidelines for optimum designs of μ1, numerical simulations could represent a powerful tool to compensate for lack of information obtained from experiments. As mentioned above and as shown in figure 1, μ1 employs permanent magnets producing a strong magnetic field of at least 0.15 T to obtain electron cyclotron resonance for 4.2-GHz microwaves. Owing to the small size, the strong magnetic field, and the perturbation of the electromagnetic fields, the Langmuir probe method is very challenging, so that the spatial distribution of plasma parameters is not readily available in experiments. Hence, we have been developing and improving a three-dimensional numerical model, which consists of a particle-in-cell simulation with a Monte Carlo collision algorithm (PIC-MCC) for the kinetics

of charged particles [7], a finite-difference time-domain (FDTD) algorithm for the electromagnetic fields of 4.2-GHz microwaves [8], and a finite element analysis for the magnetostatic fields of permanent magnets.

There are some recent papers on PIC-MCC simulations for the electric propulsion using low-temperature plasmas, such as ion thrusters [9], Hall thrusters [10-14], and high efficiency multistage plasma (HEMP) thrusters [15]. Since the scale of these thrusters is over a few centimeters, it is very time consuming to calculate high density plasmas in the discharge chambers with PIC-MCC in spite of the progress made in computer performance. To accelerate the simulation time, an artificial ion to electron mass ratio and/or an artificial vacuum permittivity are usually used to simulate plasma discharges. However, the mass ratio manipulation distorts the physics of electron transport across the magnetic field, and if the vacuum permittivity is artificially increased, the Debye length increases and then the plasma oscillation slows down. Hence, incorrect result may be obtained as long as these artificial parameters are employed.

In our case, we take advantage of the small size of μ1 as shown in figure 1, and thus we take into account the real mass ratio and the real vacuum permittivity in the present model developed. Since it is difficult to conduct plasma diagnostics of μ1 because of its structure, a visualized model of μ1 shown in figure 2 was developed for diagnostics, where a cuboid discharge chamber is employed. The chamber consists of the metal and glass walls and a pseudo grid system, the conductance of which is the same as that of the μ1 grid system. Here,

the glass wall is used for observation and laser absorption spectroscopy (LAS) [16]. Although the LAS diagnostics is now in progress and not included in the present paper, the visual appearance of the plasma discharge is compared with numerical results. The visualized model of μ1 will be referred to as the VM1 from now on. The next section describes the model developed for the VM1, which is fundamentally based on our previous papers for a micro RF ion thruster [17] and a miniature inductively coupled plasma source [18, 19]. The numerical results are then given and discussed in section 3. Finally, conclusions are drawn in section 4 of this paper.

2. Numerical model

2.1. Configuration

Figure 3 shows the computational domain and grids of the VM1 in this study. Cartesian coordinate system is employed and its origin is placed on the centre of the antenna at the interface between the metal wall and the plasma in z direction. Both lengths in the x and y directions are set at 20 mm and the length in the z direction is 4 mm. The transverse electromagnetic (TEM) waves are injected into the system at the excitation plane ($z = -1.2$ mm) of the coaxial waveguide, the inside of which is filled with the dielectric of boron nitride (BN). The microwave power is fed to the ring antenna through the four spokes as shown in figure 3(a). It should be noted that the BN region is also included in the electromagnetic-field calculation of microwaves, although the simulation area for charged particles is only the

plasma region. The grid spacing is set at 0.2 mm at regular intervals. For the plasma parameter range calculated in the present study, the grid spacing (Δx, Δy, and Δz) is small enough to satisfy the condition: the Debye length λ_D is roughly larger than $\Delta x/3$, $\Delta y/3$, and $\Delta z/3$ [20]. As shown in figure 8(b) (also see figure 9 in [21]), the plasma discharge can hardly be observed in the region between the antenna and the ring magnets especially at low powers (< 1 W). The discharge characteristics is not considered to be influenced significantly by the space between inner and outer ring magnets; and thus the space is neglected and filled with metal for simplicity.

2.2. Assumption

Our PIC-MCC model generally follows the methodology described in our previous papers [17-19]. The present model has the following general assumptions.

(i) Only Xe ions and electrons are treated as particles, and the ion species of interest is singly-ionized Xe^+ only.

(ii) Neutral particles are spatially uniform throughout the simulation and have Maxwellian velocity distribution at a gas temperature of 300 K (= 0.026 eV). The effect of neutral gas heating is not included in the simulation as indicated in [22].

(iii) The reactions taken into account are elastic scattering, excitation, and ionization for electrons, and elastic scattering and charge exchange for ions, as below.

a. $e + Xe \rightarrow e + Xe$ (Elastic Scattering)

b. $e + Xe \rightarrow e + Xe^*$ (Excitation)

c. $e + Xe \rightarrow e + Xe^+ + e$ (Ionization)

d. $Xe^+ + Xe \rightarrow Xe + Xe^+$ (Charge Exchange)

e. $Xe^+ + Xe \rightarrow Xe^+ + Xe$ (Elastic Scattering)

(iv) The motion of excited-state atoms is not considered.

(v) Coulomb collisions are not taken into account.

(vi) The magnetic fields of microwaves are neglected compared with the magnetostatic fields of the permanent magnets.

(vii) Since we have conducted calculations for a low power of microwaves at this stage, the plasma current is assumed to be neglected. The electromagnetic fields of microwaves and the electrostatic fields due to the space charge of charged particles are solved separately, and therefore self-consistent electromagnetic fields are not obtained strictly.

2.3. Electrostatic field

The electrostatic field $\boldsymbol{E}_{\mathrm{ES}}$ is given by

$$\boldsymbol{E}_{\mathrm{ES}} = -\nabla\phi, \tag{1}$$

with the potential ϕ. The potential ϕ is derived from the space charge of charged particles. The Poisson equation is given by

$$\left(\frac{\partial^2}{\partial x^2} + \frac{\partial^2}{\partial y^2} + \frac{\partial^2}{\partial z^2}\right)\phi(x,y,z) = -\frac{\rho(x,y,z)}{\varepsilon_0}, \tag{2}$$

where ρ is the charge density. Equation (2) is solved by using the method of successive-over-relaxation (SOR) with boundary conditions of zero at all the walls. Once the potential is obtained, the electrostatic field is determined by the central difference from the potential. It should be noted that we apply a digital smoothing algorithm to the space charge in order to decrease the numerical noise owing to the limited number of superparticles [23].

2.4. Electromagnetic field

The electromagnetic fields $\boldsymbol{E}_{\mathrm{EM}}$ of microwaves are obtained by solving Maxwell's equations [equations (3) and (4)] using FDTD approximation.

$$\nabla \times \boldsymbol{E}_{\mathrm{EM}} = -\frac{\partial \boldsymbol{B}}{\partial t}, \tag{3}$$

$$\nabla \times \boldsymbol{B} = \mu_0 \left(\boldsymbol{j} + \varepsilon_{\mathrm{r}} \varepsilon_0 \frac{\partial \boldsymbol{E}_{\mathrm{EM}}}{\partial t} \right), \tag{4}$$

where $\boldsymbol{B}$ is the magnetic fields of microwaves, $\boldsymbol{j}$ the plasma current density, ε_0 the electric permittivity of vacuum, ε_{r} the relative permittivity, μ_0 the magnetic permeability of vacuum. The relative permittivity ε_{r} is set at 1 in the plasma and 4.5 in the dielectric of BN. The electric field components normal to metal surfaces are set to be zero.

2.5. Motion and collisions of charged particles

Using the electrostatic field and electromagnetic field obtained above, we move charged particles by integrating the equation of motion:

$$\frac{d\boldsymbol{v}}{dt} = \frac{q}{m}(\boldsymbol{E}_{\mathrm{ES}} + \boldsymbol{E}_{\mathrm{EM}} + \boldsymbol{v} \times \boldsymbol{B}_{\mathrm{st}}), \tag{5}$$

where q is the charge, m the electron/ion mass, and $\boldsymbol{v}$ the velocity of charged particles. It should be noted that the electric fields is the sum of $\boldsymbol{E}_{\mathrm{ES}}$ and $\boldsymbol{E}_{\mathrm{EM}}$, and only the magnetostatic fields of the permanent magnets $\boldsymbol{B}_{\mathrm{st}}$ is taken into account because the magnetic fields of microwaves $\boldsymbol{B}$ is negligibly small compared with $\boldsymbol{B}_{\mathrm{st}}$ as will be shown later in section 3.1. Here, the magnetostaic fields are determined with ANSYS Emag$^{\mathrm{TM}}$ software. Since the motion of ions is much slower than microwave oscillations, the time-averaged electric field over one microwave cycle $\boldsymbol{E}_{\mathrm{av}}$ instead of $\boldsymbol{E}_{\mathrm{ES}} + \boldsymbol{E}_{\mathrm{EM}}$ is used to advance the velocity of ions.

Equation (5) is solved by Buneman-Boris method [20], and motion and collisions of charged particles can be treated separately by the principle of decoupling if a chosen time step gives a small collision probability [24]. To reduce the cost of calculation time, we employ the null-collision method [25] in MCC with cross sections for electrons [26-28] and ions [29]. The postcollision velocities of electrons and ions are determined by the use of the conservation equations for momentum and energy [24]. We employ fully absorbing walls as the boundary condition for both electrons and ions, so that all electrons and ions disappear at the walls and the antenna.

2.6. Numerical procedures and additional remarks

First, the electromagnetic fields of microwaves injected are calculated with a time increment $\Delta t_{\mathrm{EM}} = 2.98 \times 10^{-13}$ s (1/800 of a microwave cycle for 4.2 GHz) for a time span of typically

several microwave periods to obtain a steady state of the electromagnetic fields without plasma. Second, PIC-MCC calculations are performed with a time step $\Delta t_e = 5.95 \times 10^{-12}$ s (1/40 of a microwave cycle) by using the time-varying electric field of $\boldsymbol{E}_{EM}(t) = |\boldsymbol{E}_{EM}|\cos(2\pi ft)$. The time step Δt_e is sufficient to resolve the electron plasma frequency and is much smaller than the mean free time. Here, in order to speed up the simulation, the motion of ions is updated with a time step $\Delta t_i = 2.38 \times 10^{-10}$ s (one microwave cycle) by neglecting $\boldsymbol{E}_{EM}$ and using the time-averaged $\boldsymbol{E}_{ES}$ because the frequency of 4.2 GHz is much higher than the ion plasma frequency. The time-averaged kinetic power deposition is recorded by calculating the change in kinetic energy of electrons and ions before and after each charged particle is moved on integrating the equation of motion [30]. In the simulation, the power absorbed in the plasma P_{abs} is used as an input parameter. Last, we rescale the amplitude $|\boldsymbol{E}_{EM}|$ to yield the specified power absorbed in the plasma and iterate the above procedure until the steady state solution is obtained. Here, we monitor the volume-averaged electron and ion densities as a function of time, and decide that the calculation has reached the steady state when the fluctuation of the averaged densities is less than a few percent. The total computational time under the base case condition described in section 3.1 is about a week on a workstation with four 3.0-GHz processors and 12 GB of memory.

For PIC-MCC calculations, spatially uniform ions and electrons with Maxwellian velocities are loaded in the simulation area, where the initial number of electron and ion superparticles is set at 1000000. When the number exceeds or falls below a predefined limit

owing to their ionization or disappearance at the boundaries, the number of superparticles is adjusted to around the initial number in the same manner as described in [31]. One might expect that the number of superparticles is too low to conduct PIC-MCC simulations. However, the plasma frequency ω_{pe} is much larger than the collision frequency ν ($\nu/\omega_{pe} < 10^{-2}$) because of low pressure plasmas in our case, and thus the self-heating time is quite large [32]. We have also confirmed that there were no differences in the numerical results although the number of superparticles per cell volume was quadrupled. In addition, we have conducted a PIC-MCC simulation with the grid spacing of 100 μm and we have almost the same sheath thickness and position where the peak density is obtained although there is a slight difference in distributions. To reduce the computational time, we employ the grid spacing of 200 μm in the present paper; and thus the discussion is limited to the qualitative characteristics of plasma discharges. Moreover, the relatively rough grid spacing limits our calculation conditions. If the absorbed power P_{abs} increases, the plasma density also increases, which results in the decrease in the Debye length. The grid spacing is not small enough to satisfy the condition as described in section 2.1. The maximal P_{abs} we can simulate is less than 0.8 W in the present study.

3. Numerical results and discussion

3.1. Base case condition

A xenon plasma discharge was calculated for the VM1 shown in figure 3 under the base case

condition, where the xenon gas pressure is p = 1 mTorr, the microwave frequency is f = 4.2 GHz, and the absorbed power is P_{abs} = 0.3 W. The initial densities of both electrons and ions are set at 1.0 × 10^{16} m^{-3} and are distributed uniformly in the simulation area. The initial electron and ion temperatures are 2.0 and 0.05 eV, respectively. The macroscopic parameters, such as the electron density and electron temperature, shown below were determined by averaging over 50,000 microwave cycles (11.9 μs) after the steady state was reached.

Figure 4 shows typical snapshots of the electric fields of microwaves at the x-y plane (z = 2.0 mm) and z-y plane (x = 0.0 mm), taken at the time when the electric fields reach the maximal values in a microwave period. The figure indicates the peak electric field near the circumference of the microwave antenna, especially between the antenna and the permanent magnets. The electric field in the z direction E_z is larger than the other components of the electric fields. The electric field in the x direction E_x is zero at x = 0 plane because of the symmetry, and thus E_z is dominant on the right side of the ring antenna at the z-y plane of x = 0 mm.

Figure 5 shows the strength of the magnetic field $|\boldsymbol{B}_{st}|$ of permanent magnets and the magnetic field lines, together with the thick lines in red representing the resonant magnetic field of 0.15 T for 4.2-GHz microwaves. Here, the coercivity of the magnets and the relative permeability of the yoke are set at 780 kA/m and 2000, respectively. As shown in the figure, the magnetic field in the y direction B_y around ring antenna (between y = 4 mm and y = 6 mm) is dominant. These results in figures 4 and 5 indicate that electrons can be effectively heated

in the ECR layer on the right side of the ring-shaped antenna. Typical snapshots of the magnetic fields of microwaves at the *x*-*y* plane (z = 2.0 mm) are also shown in figure 6, taken at the same time as in figure 4. Compared with the strength of the magnetic field $|\boldsymbol{B}_{st}|$ of permanent magnets as shown in figure 5, the strength of the magnetic field of microwaves is quite small by three orders of magnitude, and thus only the magnetostatic fields of the permanent magnets $\boldsymbol{B}_{st}$ is taken into account in equation (5).

Figure 7 shows an example of the electron trajectory near the ECR layer. The electron moves along the magnetic field line and travels back and forth as a result of the confinement due to the mirror magnetic fields; the electron gains the energy from microwaves during this motion because of the ECR. Moreover, the grad-B and/or curvature drift is also confirmed in figure 7(b). The energy of electrons can be high enough to exceed the threshold energy of the ionization (12.1 eV) owing to heating in the ECR layer as shown in figure 7(c), and therefore ring-shaped plasma discharges are expected to be generated and maintained in front of the ring antenna.

Shown in figure 8(a) is the photograph image at the *x*-*y* plane of μ1 in plasma-discharging operation taken from the downstream of the thruster under the condition of 1 W microwave power with the xenon gas flow rate of 0.15 sccm. The ring-shaped plasma discharge was confirmed behind the grid electrodes as expected. Figure 9 shows the three-dimensional distribution of the time-averaged electron density. As shown in these figures, the peak plasma density is located in the ECR layer on the right side of the antenna,

where the maximal value of the electron density is 1.6×10^{17} m^{-3}, and their distributions spread along the magnetic field lines. This result indicates that the plasma is well confined because of the mirror magnetic fields, and such distribution can also be seen in figure 8(b) showing the photograph image at the *y*-*z* plane of the VM1 under the condition of 0.79 W microwave power with the xenon gas flow rate of 0.12 sccm. The brightest region of the plasma discharge coincides well with the region where the peak plasma density is obtained. The distribution of the electron density is also almost the same as that of the ion density (not shown here), indicating that quasi-neutrality is confirmed. Although our simulation model cannot be validated just by comparing the electron density profile of the calculation with the visual appearance of the plasma discharge in experiments, the simulation result also produces the ring-shaped profile of the plasma density.

Figure 10 shows the three-dimensional distributions of the time-averaged electron temperature, where the electron temperature T_e is defined by the following equation with the number of superparticles N.

$$T_e = \frac{N}{3(N-1)} \frac{m}{q} \left(\frac{1}{N} \sum v^2 - \left(\frac{1}{N} \sum v \right)^2 \right). \quad (6)$$

The distribution of the electron temperature is almost the same as that of the plasma density, where the peak electron temperature obtained is 16 eV. The electron temperature in front of the ring antenna is much larger than the ionization energy of xenon. Since the temperature defined by equation (6) is just a macroscopic parameter, a large population of high-energy electrons is expected, which will be described below in section 3.2. The three-dimensional

distributions of the time-averaged potential are also shown in figure 11, where the peak plasma potential obtained is 21 V and its location is similar to that of electron density. However, the potential has a little broad peak compared with the plasma density and the electron temperature, owing to the diffusion characteristic of equation (2).

We are not able to measure the distribution of plasma parameters with a probe inside the discharge chamber at this stage. In our previous paper [33], however, a guardring probe was aligned on the inner surface of the metal wall just downstream of the ECR region, corresponding to the position of x = 0, y = 5, z = 4 mm in figures 9 and 10. The plasma density was calculated to be 0.29×10^{17} m^{-3} at a net power absorbed in the plasma of 0.3 W by using the ion saturation current and a measured electron temperature of T_e = 10 eV. Although the discharge chamber was composed of glass tube and a metal mesh in [33], the other dimensions are almost the same as the VM1, and thus our simulation results would not off by more than one order of magnitude compared with experimental results.

Figures 12 and 13 indicate the three-dimensional distributions of the time-averaged ionization rate and excitation rate, respectively. Since the threshold energy of ionization is higher than that of excitation and the cross section of the ionization is larger than that of excitation at higher electron energy (> 22 eV) [13], the maximal value of the ionization rate is larger than that of the excitation rate and the distribution of the ionization rate is more localized in the ECR layer. On the other hand, the excitation rate is distributed a little more broadly. It should be noted that their values equal to zero are not plotted for visibility.

Table 1 summarizes power balance results. The total power absorbed by the plasma P_{abs} is due to the electron heating P_e and ion heating P_i, whereas the total power lost by the plasma P_{loss} is equal to the sum of the power loss of electron and ion to the walls ($P_{e,wall}$ and $P_{i,wall}$), and collisions with neutral particles. Here the collision losses are elastic scattering, excitation, and ionization for electrons ($P_{e,elas}$, $P_{e,exc}$, and $P_{e,ion}$), and elastic scattering and charge exchange for ions ($P_{i,elas}$ and $P_{i,cex}$). The power absorbed by the plasma P_{abs} and the power lost by the plasma P_{loss} agree to within 1%. We also see similar good agreement between P_e and $P_{loss,e}$ and between P_i and $P_{loss,i}$. The dominant component of the power absorption is attributed to the electron motion. However, power absorption due to the ion motion cannot be neglected, especially in the z direction, not toward the side wall (x and y directions). This is because that the ions are accelerated through the potential drop in the sheath and lose their energy on the wall, and the most of the region where the high plasma density is obtained is close to the wall in the z direction as shown in figure 9. For the ion thruster of μ1, the metal wall at z = 4 mm is actually a grid electrode to accelerate ions through it. Hence, the ions are expected to be accelerated effectively through the grid electrode without a large loss of ions toward side walls. Although the electrons also lose their energy on the wall because of the large surface-to-volume ratio, the power dissipation of ionization is much larger than that of excitation. This result is consistent with the results shown in figures 12 and 13.

3.2. Power dependence

Figure 14 shows the three-dimensional distributions of the time-averaged electron density, electron temperature, and potential at the absorbed power P_{abs} = 0.5 and 0.7 W. The peak electron density increases almost linearly with increasing absorbed power, leading to the increase in the peak potential. However, the peak electron temperature is almost constant for all the absorbed powers while the distribution of high electron temperature spreads over a wider area with an increase in power. This tendency is also confirmed in the electron density and potential, where the increasing rate at the centre area is a little larger than that at the ECR area.

Figure 15 shows the normalized electron energy probability functions (EEPFs) at the centre and ECR areas for the absorbed powers of 0.3, 0.5 and 0.7 W. Here, the definition of the EEPF is the same as in our previous papers [18, 19]. As shown in the figure, depletion of EEPF can be seen at the centre owing to the inelastic collision loss and low power absorption from microwaves. However, the ECR produces a large number of high-energy electrons, resulting in a high degree of ionization in the ECR layer. This large difference in EEPFs at different points leads to the plasma distributions shown above. Moreover, the difference in EEPFs at centre area is larger than that at ECR area. These differences in EEPFs are consistent with the power dependence of the distributions of electron temperature. It should be noticed that the number of high energy electrons at the ECR region is overestimated in the EEPFs because (electron-electron) Coulomb collisions are not taken into account as describe

in section 2.2. The EEPFs would be closer to Maxwellian owing to the relaxation of electron-electron collisions if the effect of Coulomb collisions was considered [34, 35].

The saturation of the peak electron temperature implies that the mirror magnetic fields cannot confine high energy electrons effectively. However, too high electron temperature would produce a large number of doubly charged ions, which degrades the thruster efficiency. Moreover, more uniform distribution of plasma density is desirable to produce higher thrust densities, and thus the increase in plasma density at the centre area is preferred. A magnetic field configuration which confines outward electrons but releases inward electrons might produce a better thruster performance.

4. Conclusions

In the present work, we have developed a three-dimensional PIC-MCC model for a miniature microwave discharge ion thruster VM1 to elucidate the mechanism of ECR discharges confined in a small space. The PIC-MCC results have shown that the electrons are well confined owing to the mirror magnetic fields and can be effectively heated in the ECR layer downstream of the ring antenna because of the configuration of the magnetostatic fields and microwave electric fields. The confinement results in the ring-shaped profiles of the plasma density along the antenna. The visual appearance of the plasma discharge of the thruster in operation was also ring-shaped. Moreover, the results of power balance and power dependence imply that the ions are expected to be accelerated effectively through the grid

electrode and more uniform ion beam distribution can also be expected. In future work, the plasma current and the doubly charged ions are also taken into account in our model and plasma characteristics at nominal power range will be calculated and compared with experimental results [16].

Acknowledgments

This work was financially supported in part by a Grant-in-Aid for Scientific Research (B), 25289304, from the Japan Society for the Promotion of Science.

References

[1] Micci M M and Ketsdever A D 2000 *Micropropulsion for small spacecraft* (Reston: American Institute of Aeronautics and Astronautics)

[2] Koizumi H and Kuninaka H 2010 Miniature microwave discharge ion thruster driven by 1 watt microwave power *J. Propul. Power* **26** 601-604

[3] Koizumi H and Kuninaka H 2010 Switching operation of ion beam extraction and electron emission using the miniature ion thruster μ1 *Trans. JSASS Aerospace Tech. Japan* **8** Pb_85-Pb_90

[4] Kuninaka H and Satori S 1998 Development and demonstration of a cathodeless electron cyclotron resonance ion thruster *J. Propul. Power* **14** 1022-1026

[5] Kuninaka H, Nishiyama K, Funaki I, Yamada T, Shimizu Y and Kawaguchi J 2007 Powered flight of electron cyclotron resonance ion engines on hayabusa explorer *J. Propul. Power* **23** 544-551

[6] Koizumi H, Komurasaki K and Arakawa Y 2012 Development of the miniature ion propulsion system for 50 kg small spacecraft *Proc. 48th AIAA/ASME/SAE/ASEE Joint Propulsion Conference & Exhibit* (Atlanta, Georgia, USA) AIAA-2012-3949

[7] Birdsall C K 1991 Particle-in-cell charged-particle simulations, plus monte carlo collisions with neutral atoms, pic-mcc *IEEE Trans. Plasma Sci.* **19** 65-85

[8] Yee K 1966 Numerical solution of initial boundary value problems involving maxwell's equations in isotropic media *IEEE Trans. Antennas Propagat.* **14** 302-307

[9] Mahalingam S and Menart J A 2010 Particle-based plasma simulations for an ion engine discharge chamber *J. Propul. Power* **26** 673-688

[10] Liu H, Wu B, Yu D, Cao Y and Duan P 2010 Particle-in-cell simulation of a hall thruster *J. Phys. D: Appl. Phys.* **43** 165202-1-9

[11] Coche P and Garrigues L 2014 A two-dimensional (azimuthal-axial) particle-in-cell model of a hall thruster *Phys. Plasmas* **21** 023503-1-10

[12] Yu D, Song M, Liu H, Ding Y J and Li H 2012 Particle-in-cell simulation of a double stage hall

thruster *Phys. Plasmas* **19** 033503-1-7

[13] Szabo J, Warner N, Martinez-Sanchez M and Batishchev O 2014 Full particle-in-cell simulation methodology for axisymmetric hall effect thrusters *J. Propul. Power* **30** 197-208

[14] Cho S, Komurasaki K and Arakawa Y 2013 Kinetic particle simulation of discharge and wall erosion of a hall thruster *Phys. Plasmas* **20** 063501-1-12

[15] Zhao Y J, Liu H, Yu D R, Hu P and Wu H 2014 Particle-in-cell simulations for the effect of magnetic field strength on a cusped field thruster *J. Phys. D: Appl. Phys.* **47** 045201-1-8

[16] Sugita Y, Koizumi H, Tsukizaki R, Kuninaka H, Takao Y, Yamagiwa Y and Matsui M 2013 Plasma diagnostics in a miniature microwave discharge ion thruster *Proc. 33rd International Electric Propulsion Conference* (Washington, D.C., USA) IEPC-2013-245

[17] Takao Y, Sakamoto M, Eriguchi K and Ono K 2014 Investigation of plasma characteristics and ion beam extraction for a micro rf ion thruster *Trans. JSASS Aerospace Tech. Japan* **12** Pb_13-Pb_18

[18] Takao Y, Eriguchi K and Ono K 2012 Effect of capacitive coupling in a miniature inductively coupled plasma source *J. Appl. Phys.* **112** 093306-1-10

[19] Takao Y, Kusaba N, Eriguchi K and Ono K 2010 Two-dimensional particle-in-cell monte carlo simulation of a miniature inductively coupled plasma source *J. Appl. Phys.* **108** 093309-1-8

[20] Birdsall C K and Langdon A B 1991 *Plasma physics via computer simulation* (Bristol, U.K.: IOP Publishing)

[21] Koizumi H and Kuninaka H 2009 Antenna design method and performance improvement of a micro ion engine using microwave discharge *Trans. JSASS Space Tech. Japan* **7** Pb_89-Pb_94

[22] Nam S K and Economou D J 2004 Two-dimensional simulation of a miniaturized inductively coupled plasma reactor *J. Appl. Phys.* **95** 2272-2277

[23] Verboncoeur J P 2005 Particle simulation of plasmas: Review and advances *Plasma Phys. Control. Fusion* **47** A231-A260

[24] Nanbu K 2000 Probability theory of electron-molecule, ion-molecule, molecule-molecule, and coulomb collisions for particle modeling of materials processing plasmas and cases *IEEE Trans. Plasma Sci.* **28** 971-990

[25] Vahedi V and Surendra M 1995 A monte carlo collision model for the particle-in-cell method: Applications to argon and oxygen discharges *Comput. Phys. Commun.* **87** 179-198

[26] Hayashi M 1983 Determination of electron-xenon total excitation cross-sections, from threshold to 100 ev, from experimental values of townsend's α *J. Phys. D: Appl. Phys.* **16** 581-589

[27] Heer F J d, Jansen R H J and Kaay W v d 1979 Total cross sections for electron scattering by ne, ar, kr and xe *J. Phys. B: At. Mol. Phys* **12** 979-1002

[28] Rapp D and Englander-Golden P 1965 Total cross sections for ionization and attachment in gases by electron impact. I. Positive ionization *J. Chem. Phys.* **43** 1464-1479

[29] Boyd I D 2004 Modeling of the near field plume of a hall thruster *J. Appl. Phys.* **95** 4575-4584

[30] Surendra M and Graves D B 1991 Particle simulations of radio-frequency glow discharges *IEEE Trans. Plasma Sci.* **19** 144-157

[31] Nanbu K and Kondo S 1997 Analysis of three-dimensional dc magnetron discharge by the particle-in-cell/monte carlo method *Japan. J. Appl. Phys.* **36** 4808-4814

[32] Turner M M 2006 Kinetic properties of particle-in-cell simulations compromised by monte carlo collisions *Phys. Plasmas* **13** 033506-1-10

[33] Koizumi H and Kuninaka H 2009 Development and characterization of a low power and miniature microwave discharge plasma source *Adv. Appl. Plasma Sci.* **7** 51-54

[34] Yonemura S and Nanbu K 2001 Electron energy distributions in inductively coupled plasma of argon *Japan. J. Appl. Phys.* **40** 7052-7060

[35] Nanbu K and Yonemura S 1998 Weighted particles in coulomb collision simulations based on the theory of a cumulative scattering angle *J. Comput. Phys.* **145** 639-654

Table 1. Power balance results calculated at the absorbed power P_{abs} = 0.3 W for the pressure p = 1 mTorr.

P_{abs} (mW)	300	P_{loss} (mW)	300
$P_{\mathrm{abs,e},x}$ (mW)	57.4	$P_{\mathrm{loss,e,wall}}$ (mW)	83.2
$P_{\mathrm{abs,e},y}$ (mW)	57.6	$P_{\mathrm{loss,i,wall}}$ (mW)	111
$P_{\mathrm{abs,e},z}$ (mW)	73.1	$P_{\mathrm{loss,e,elas}}$ (mW)	0.0
$P_{\mathrm{abs,i},x}$ (mW)	11.1	$P_{\mathrm{loss,e,ex}}$ (mW)	39.0
$P_{\mathrm{abs,i},y}$ (mW)	11.0	$P_{\mathrm{loss,e,iz}}$ (mW)	65.8
$P_{\mathrm{abs,i},z}$ (mW)	89.9	$P_{\mathrm{loss,i,elas}}$ (mW)	0.2
		$P_{\mathrm{loss,i,cex}}$ (mW)	0.9

List of figure captions

Figure 1. Schematic of the microwave discharge ion thruster. The thruster consists of a cylindrical metal discharge chamber, inner/outer ring-shaped permanent magnets, yoke, coaxial waveguide, ring-shaped microwave antenna, and grid system for ion beam extraction. Two ring-shaped magnets produce the mirror magnetic fields to confine electrons and the ECR layer.

Figure 2. (a) Front (*x*-*y* plane) and (b) side (*z*-*y* plane) views of the visualized model of μ1 (VM1). The VM1 consists of the metal and glass walls and a pseudo grid system, the conductance of which is the same as that of the grid system of μ1. The glass wall is employed for visibility and laser absorption spectroscopy. Here, the cuboid discharge chamber is used for the diagnostics.

Figure 3. (a) Front (*x*-*y* plane at z =1.0 mm) and (b) side (*z*-*y* plane at x = 0.0 mm) cross-sectional views of the simulation area for the calculation of the VM1. Cartesian coordinate system is employed and its origin is placed on the centre of the antenna at the interface between the metal wall and the plasma in z direction. Both lengths in the x and y directions are set at 20 mm and the length in the z direction is 4 mm. The inside of the coaxial waveguide is filled with the dielectric of boron nitride (BN). The microwave power is fed to

the ring antenna through the four spokes. It should be noted that the BN region is also included in the electromagnetic-field calculation of microwaves, although the simulation area for charged particles is only the plasma region. The space between inner and outer ring magnets is neglected and filled with metal for simplicity of calculation.

Figure 4. Typical snapshots of the electric fields of 4.2-GHz microwaves at the (a) *x*-*y* plane (z = 2.0 mm) and (b) *z*-*y* plane (x = 0.0 mm), taken at the time when the electric fields reach the maximal values in a microwave period. The input power of microwaves is set at 0.3 W.

Figure 5. Contour plots at the *z*-*y* plane (x = 0.0 mm) of the strength of the magnetic field of the ring-shaped permanent magnets and the magnetic field lines in black, together with the thick lines in red representing the resonant magnetic field of 0.15 T for 4.2-GHz microwaves. The coercivity of the magnets and the relative permeability of the yoke are set at 780 kA/m and 2000, respectively.

Figure 6. Typical snapshots of the magnetic fields of microwaves at the *x*-*y* plane (z = 2.0 mm), taken at the same time as in figure 4. (a) $(B_x^2+B_y^2)^{1/2}$ and (b) B_z.

Figure 7. (a) Trajectory of an electron at *z*-*y* plane, together with magnetic field lines (thin lines in blue), (b) trajectory of an electron at *x*-*y* plane, and (c) the electron energy as a

function of time.

Figure 8. (a) Photograph image at the *x*-*y* plane of μ1 in plasma-discharging operation, taken from the downstream of the thruster under the condition of 1 W microwave power with the xenon gas flow rate of 0.15 sccm. (b) Photograph image at the *y*-*z* plane of the VM1 under the condition of 0.79 W microwave power with the xenon gas flow rate of 0.12 sccm.

Figure 9. Three-dimensional distributions of the time-averaged electron density n_e at each plane (left; x = 0 mm, y = 0 mm, z = 2 mm), and at the *z*-*y* plane of x = 0.0 mm (right) together with magnetic field lines (black) and ECR layer (thick lines in red) under the base case condition (f = 4.2 GHz, P_{abs} = 0.3 W, and p = 1 mTorr).

Figure 10. Three-dimensional distributions of the time-averaged electron tempearture T_e at each plane (left; x = 0 mm, y = 0 mm, z = 2 mm), and at the *z*-*y* plane of x = 0.0 mm (right) together with magnetic field lines (black) and ECR layer (thick lines in red) under the base case condition.

Figure 11. Three-dimensional distributions of the time-averaged potential ϕ at each plane (left; x = 0 mm, y = 0 mm, z = 2 mm), and at the *z*-*y* plane of x = 0.0 mm (right) together with magnetic field lines (black) and ECR layer (thick lines in red) under the base case condition.

Figure 12. Three-dimensional distributions of the time-averaged ionization rate at each plane (left; x = 0 mm, y = 0 mm, z = 2 mm), and at the z-y plane of x = 0.0 mm (right) together with magnetic field lines (black) and ECR layer (thick lines in red) under the base case condition.

Figure 13. Three-dimensional distributions of the time-averaged excitation rate at each plane (left; x = 0 mm, y = 0 mm, z = 2 mm), and at the z-y plane of x = 0.0 mm (right) together with magnetic field lines (black) and ECR layer (thick lines in red) under the base case condition.

Figure 14. Three-dimensional distributions of the time-averaged (a) electron density n_e at P_{abs} = 0.5 W, (b) n_e at P_{abs} = 0.7 W; (c) electron temperature T_e at P_{abs} = 0.5 W, (d) T_e at P_{abs} = 0.7 W; (e) potential ϕ at P_{abs} = 0.5 W, and (f) ϕ at P_{abs} = 0.7 W.

Figure 15. Normalized EEPFs at the centre and the ECR areas for the absorbed powers of 0.3, 0.5 and 0.7 W. Broken lines represent the centre area while solid lines represent the ECR area.

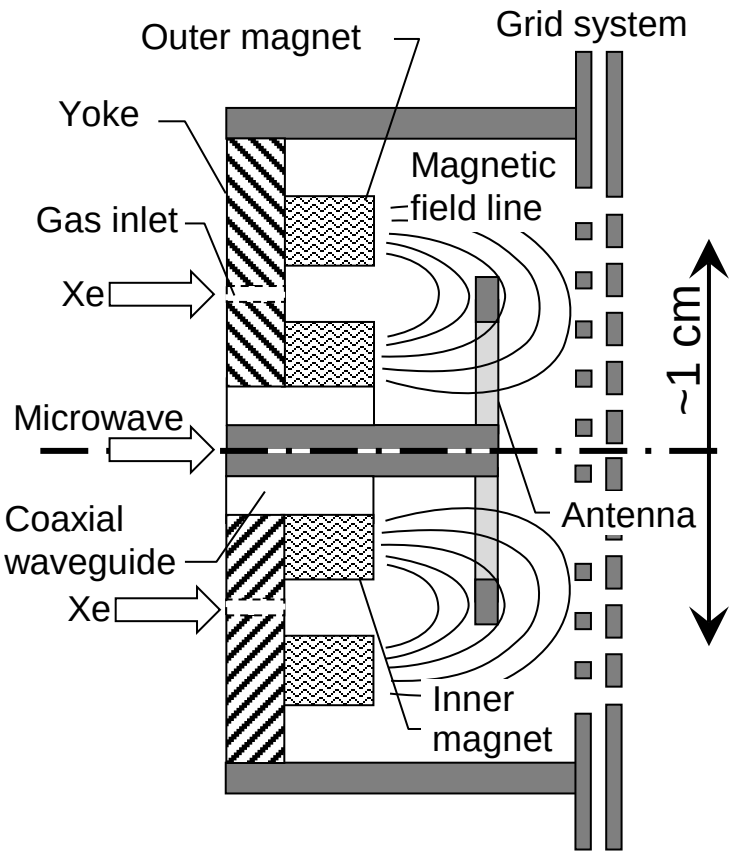

Y. Takao et al., Figure 1

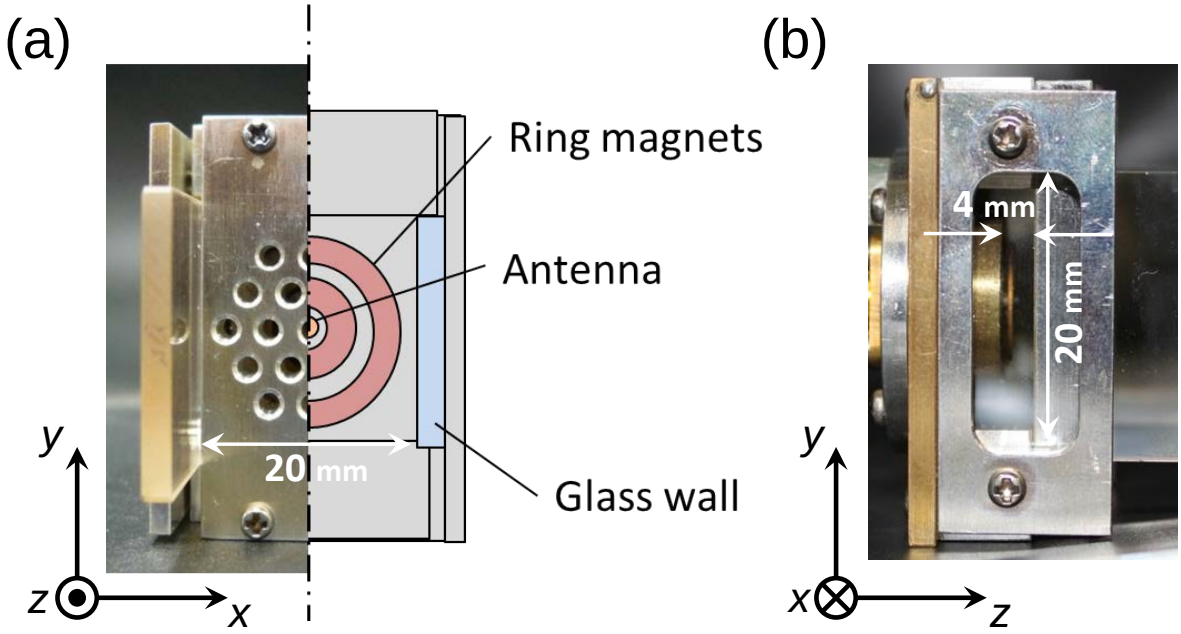

Y. Takao et al., Figure 2

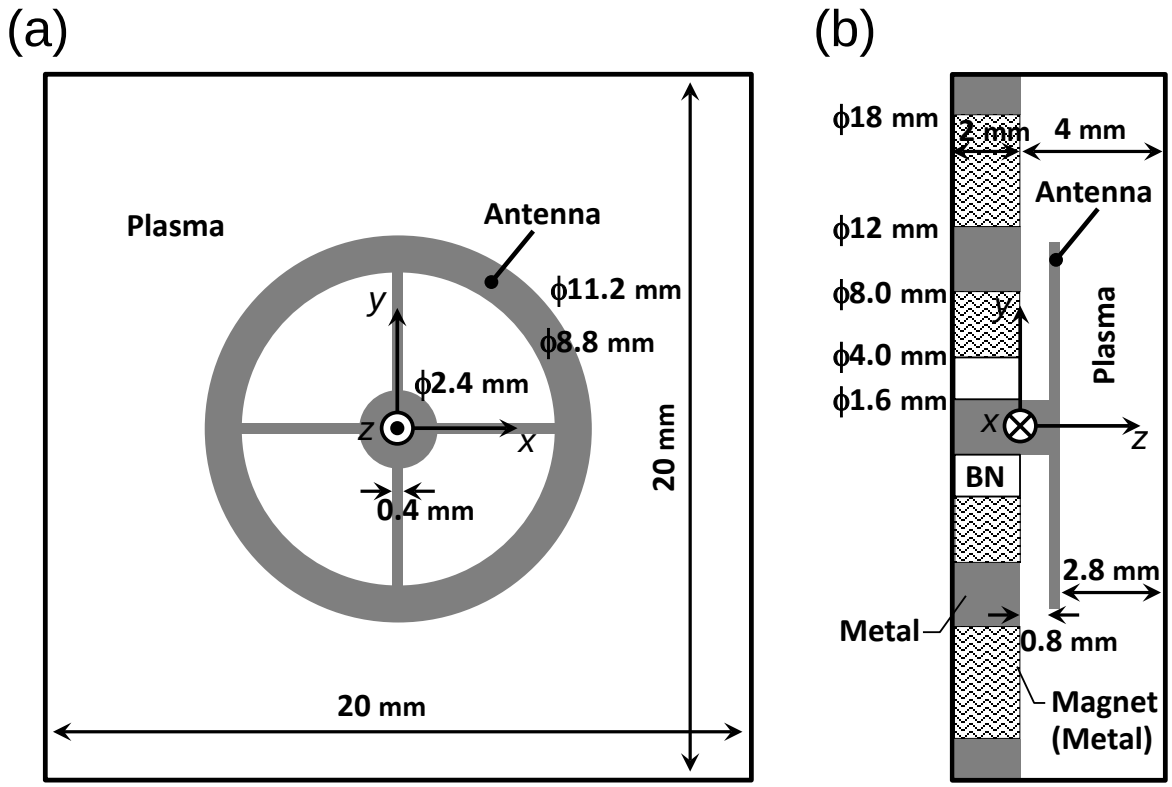

Y. Takao et al., Figure 3

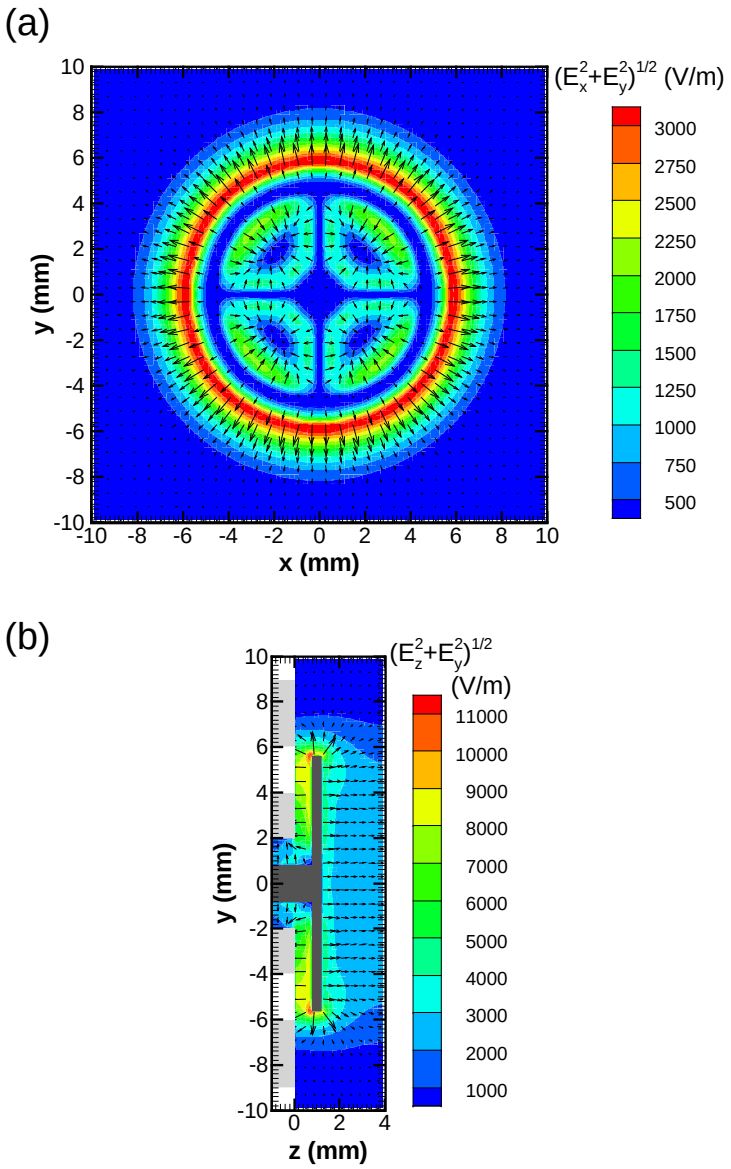

Y. Takao et al., Figure 4

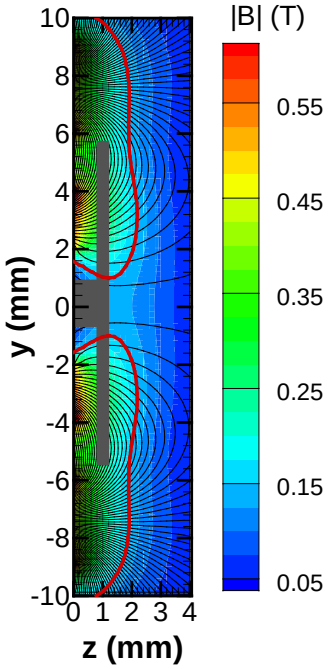

Y. Takao et al., Figure 5

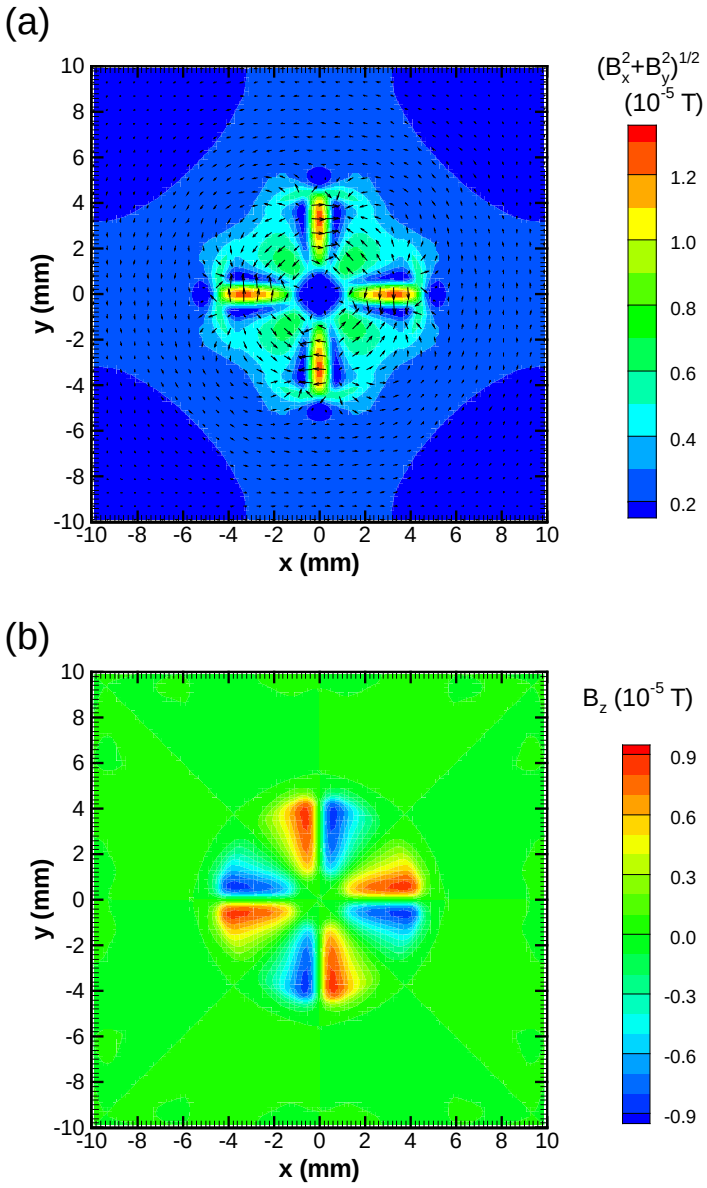

Y. Takao et al., Figure 6

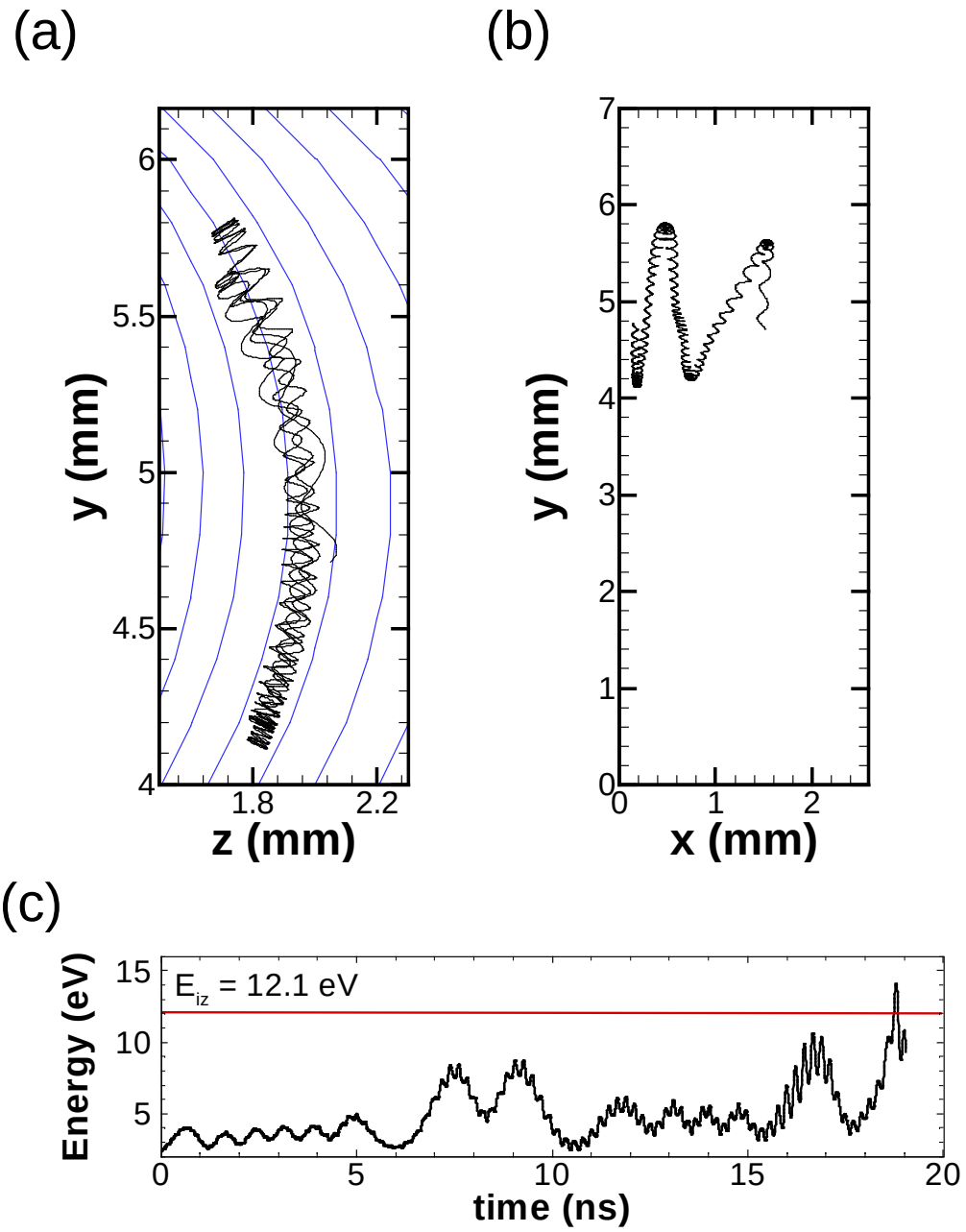

Y. Takao et al., Figure 7

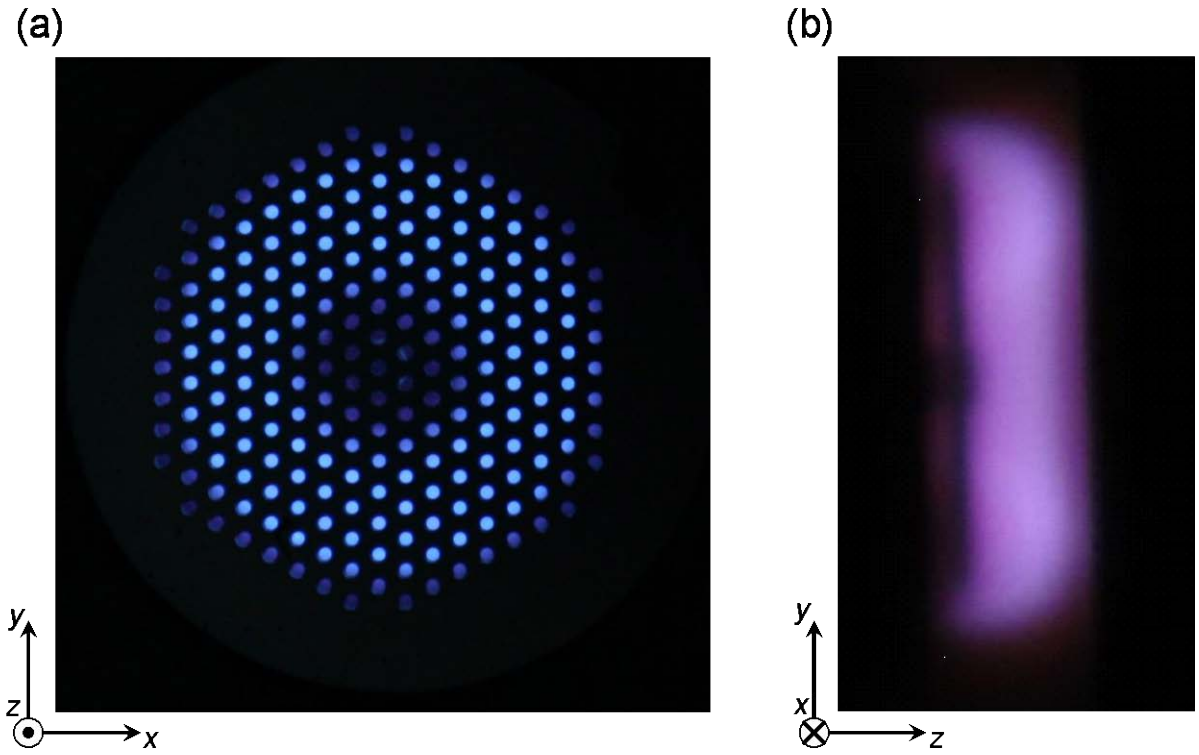

Y. Takao et al., Figure 8

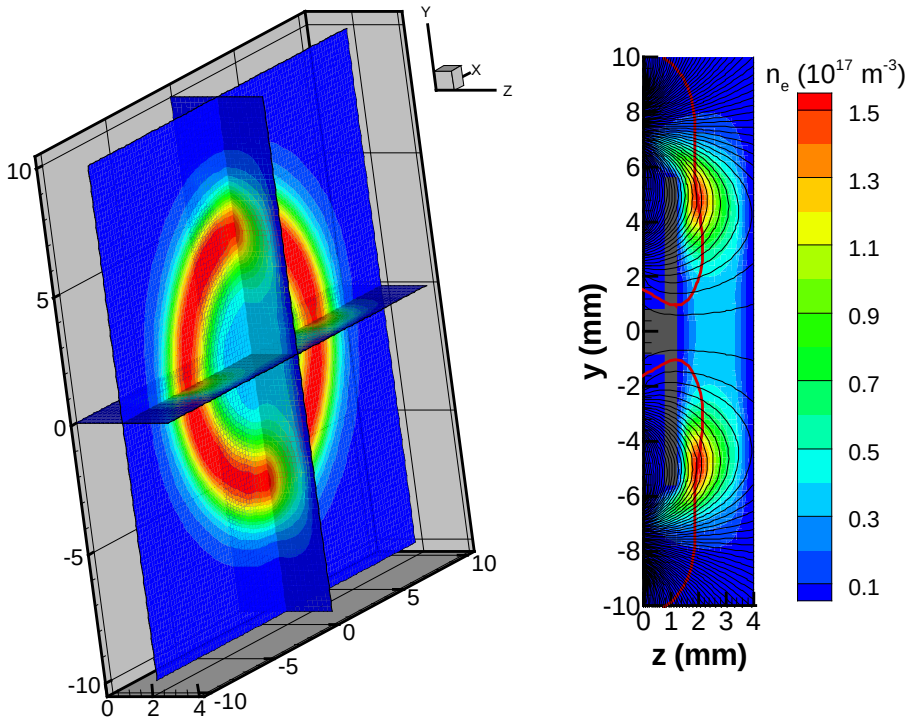

Y. Takao et al., Figure 9

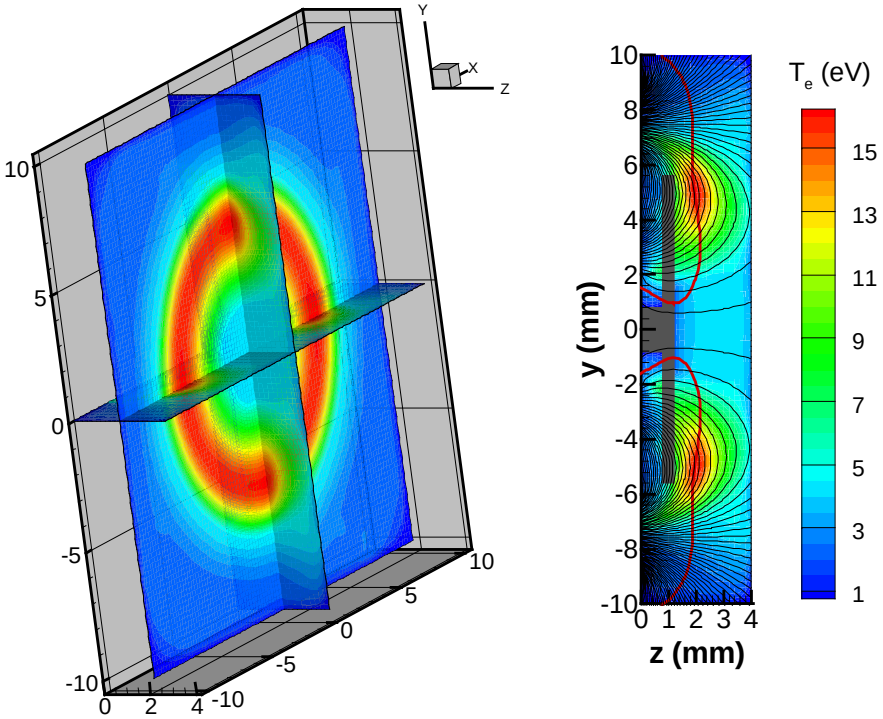

Y. Takao et al., Figure 10

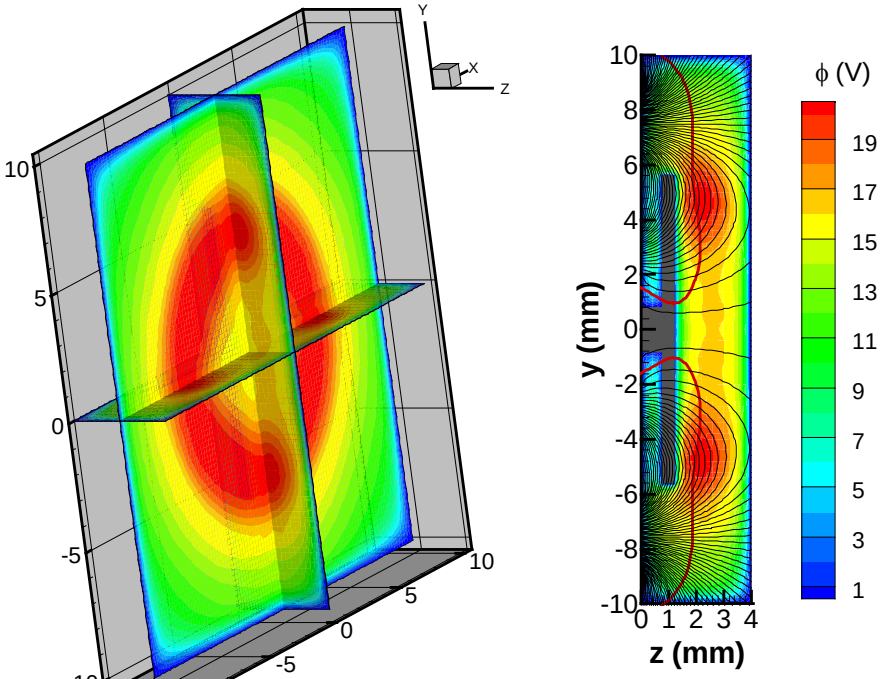

Y. Takao et al., Figure 11

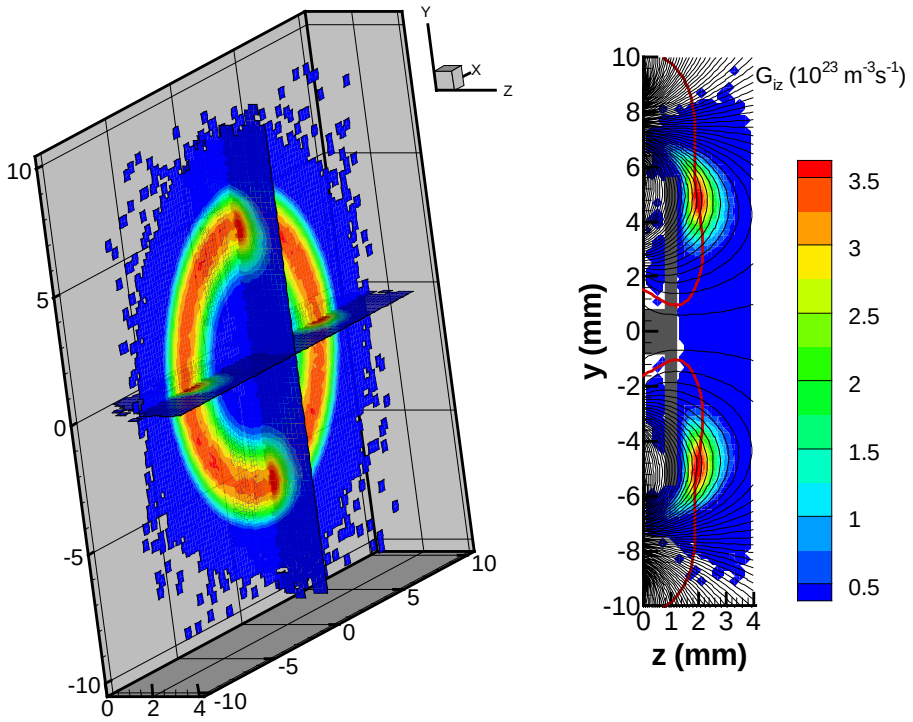

Y. Takao et al., Figure 12

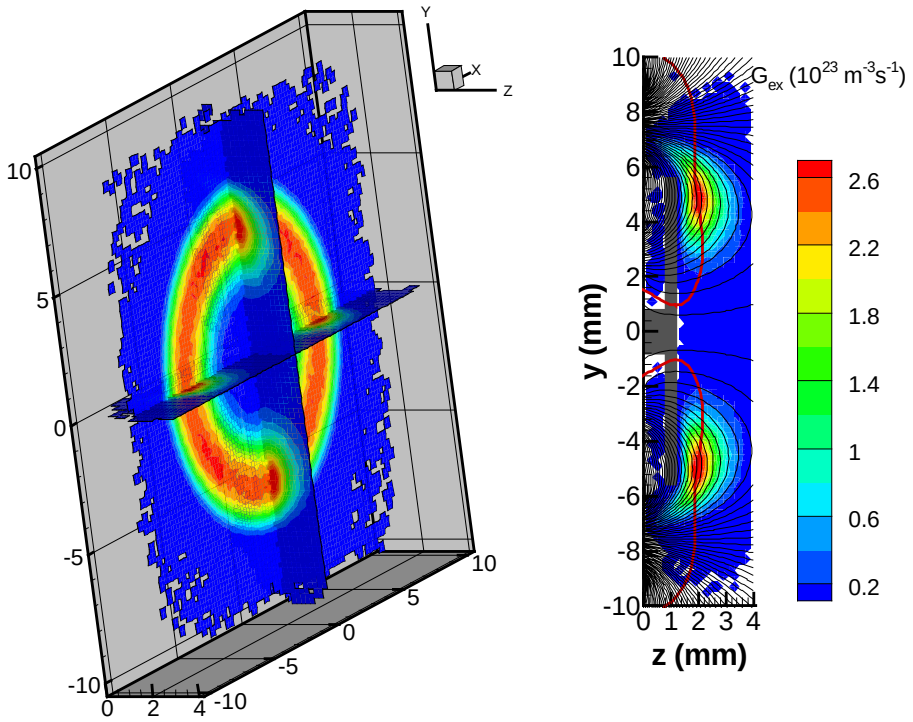

Y. Takao et al., Figure 13

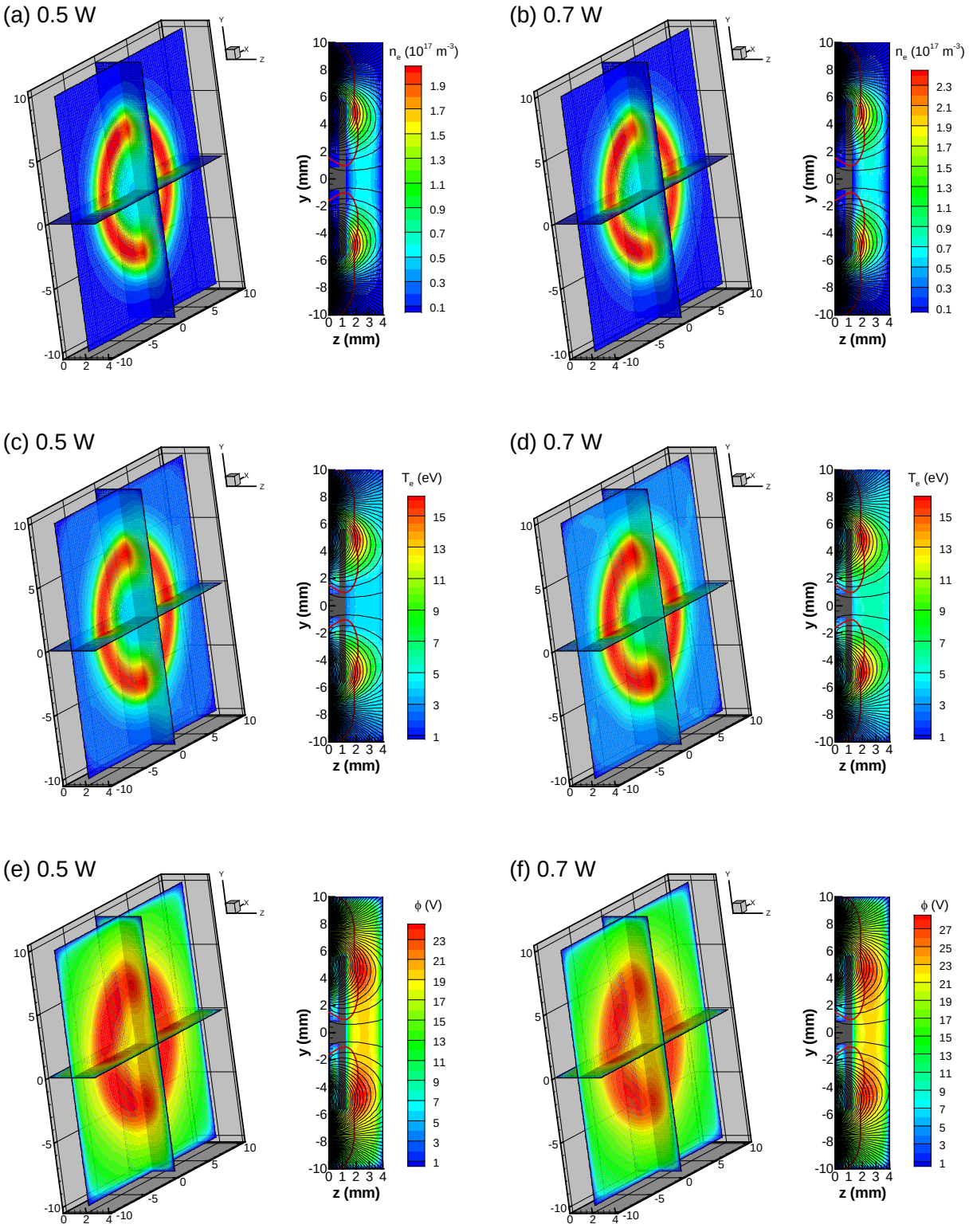

Y. Takao et al., Figure 14

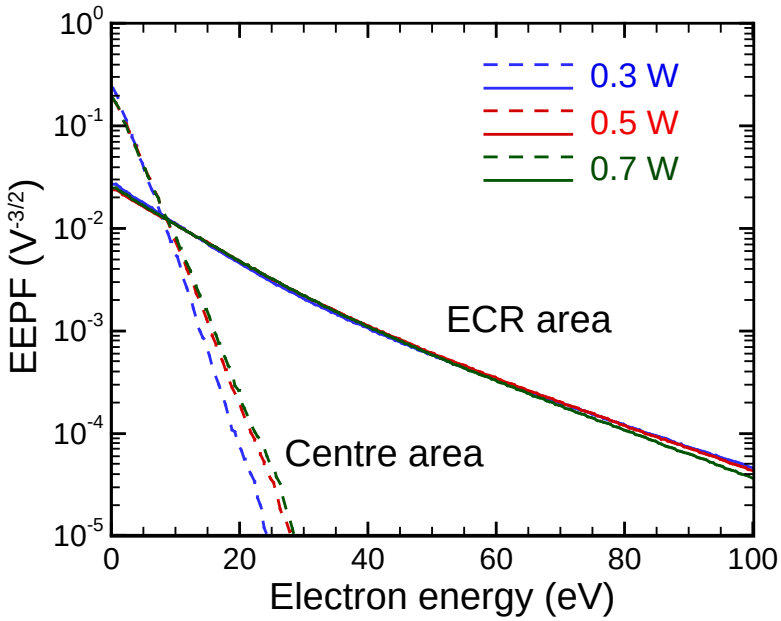

Y. Takao et al., Figure 15